Ratiometric Biosensor for Aggregation-Induced Emission-Guided Precise Photodynamic Therapy

Kai Han,[†,§] Shi-Bo Wang,[†,‡,§] Qi Lei,[†] Jing-Yi Zhu,[†] and Xian-Zheng Zhang*[,†,‡]

[†]Key Laboratory of Biomedical Polymers of Ministry of Education & Department of Chemistry and [‡]The Institute for Advanced Studies, Wuhan University, Wuhan 430072, China. [§]K.H. and S.-B.W. contributed equally.

ABSTRACT Photodynamic therapy faces the barrier of choosing the appropriate irradiation region and time. In this paper, a matrix metalloproteinase-2 (MMP-2) responsive ratiometric biosensor was designed and synthesized for aggregation-induced emission (AIE)-guided precise photodynamic therapy. It was found that the biosensor presented the MMP-2 responsive AIE behavior. Most importantly, it could accurately differentiate the tumor cells from the healthy cells by the fluorescence ratio between freed tetraphenylethylene and protoporphyrin IX (PpIX, internal reference). *In vivo* study demonstrated that the biosensor could preferentially accumulate in the tumor tissue with a relative long blood retention time. Note that the intrinsic fluorescence of PpIX and MMP-2-triggered AIE fluorescence provided a real-time feedback which guided precise photodynamic therapy *in vivo* efficiently. This strategy demonstrated here opens a window in the precise medicine, especially for phototherapy.

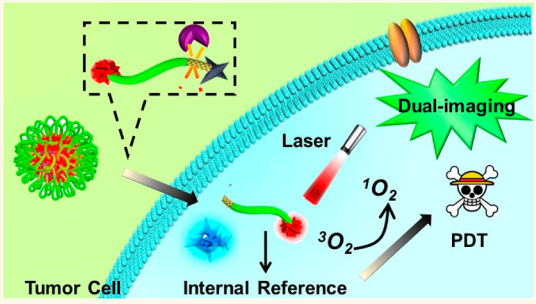

KEYWORDS: photodynamic therapy · ratiometric biosensor · MMP-2 responsive · aggregation-induced emission · tumor

Photodynamic therapy (PDT) has obtained increasing attention during the past decades, mostly because of the noninvasiveness to normal tissues as well as great potential in highly accurate tumor therapy.[1−3] Although various photodynamic therapy systems have been developed for tumor therapy, conventional photodynamic therapy systems still confront the challenge of tumor recognition. The photodynamic antitumor effect of a photosensitizer is mainly motivated by the formation of reactive oxygen species (ROS) under light irradiation.[4,5] However, the fluorescence of a photosensitizer is always "on", leading to the constant intensity as well as an abundant nonspecific signal.[6,7] Consequently, discernment of healthy cells from diseased ones became extremely difficult. Thus, choosing an appropriate irradiation region and time is highly desirable for photodynamic therapy with reduced side effects.

Recently, a new concept of "stimuli-triggered imaging" guided therapy was proposed to realize visible and precise phototherapy.[8,9] This strategy mainly utilizes specific tumor microenvironments, such as acidosis, hypoxia, and overexpressed enzymes, to activate the fluorescence signal change, which can guide the phototherapy.[10] However, fluorescence imaging response to the tumor microenvironment is basically limited to the change of fluorescence emission intensity, and fluorescence intensity is severely affected by the local content of biosensors in the tumor region as well as microenvironments.[11] As a result, the background fluorescence is always mistaken for weak fluorescence; this false positive fluorescence will cause unwanted side effects.[12] To overcome these dilemmas, a ratiometric fluorescence imaging technique has been developed to measure the fluorescence intensity ratio at two different wavelengths, which provides a built-in self-correction regardless of the local biosensor concentration and environmental affects.[13−15] However, very few studies have been done in ratiometric sensor-guided therapy,[16] and the imaging and therapy procedures were generally implemented separately. In addition, construction of ratiometric sensors is always based on the principle of a structure-changing-induced wavelength

* Address correspondence to xz-zhang@whu.edu.cn.

Received for review July 9, 2015 and accepted September 8, 2015.

Published online September 08, 2015
10.1021/acsnano.5b04243

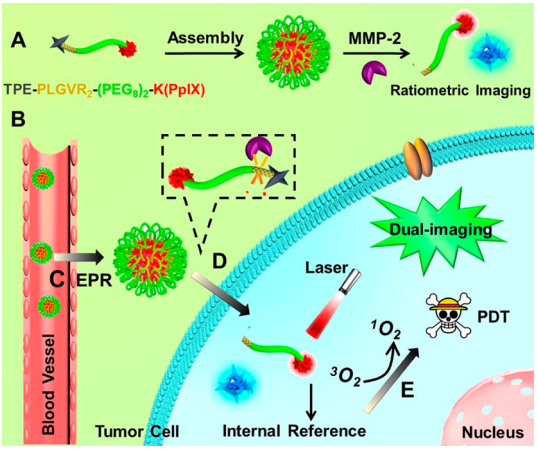

Scheme 1. (A) Self-assembly of TPPP into nanoparticles, (B) intravenous injection of TPPP into mice *via* vein injection, (C) accumulation of TPPP in the tumor region *via* enhanced permeability and retention, (D) hydrolysis of TPPP and the fluorescence recovery of TPE, and (E) AIE-guided photodynamic antitumor therapy.

shift. All of these issues make the fabrication of these nanodevices complicated and costly.[17]

Here, for the first time, we report a ratiometric fluorescence biosensor for matrix metalloproteinase-2 (MMP-2) responsive aggregation-induced emission (AIE)-guided photodynamic therapy (Scheme 1). Compared with other tumor microenvironments that are confused easily by some specific biological environments, for example, acidity also happened in an inflammation region, the overexpression of MMP-2 is a striking feature for many types of solid tumors.[18] In this report, the biosensor consisted of photosensitizer protoporphyrin IX (PpIX) and an AIE molecular tetraphenylethylene (TPE)[19−21] using the PEGylated Pro-Leu-Gly-Val-Arg (PLGVR) peptide sequence as a linker. The biosensor thus obtained was designated as TPPP (TPE-$PLGVR_2$-$(PEG_8)_2$-K(PpIX)). PpIX was employed as both the photosensitizer and fluorescence internal reference. When TPPP arrived at the tumor tissue, the overexpressed MMP-2 in the tumor region hydrolyzed the PLGVR sequence, leading to the detachment of TPE and PEGylated PpIX. The ratiometric fluorescence ratio between TPE and PpIX could evaluate the MMP-2 expression level. On the other hand, this aggregation-induced emission provided visible and accurate feedback of the photodynamic time and region. The *in vivo* antitumor effect using a nude mice model was further investigated.

RESULTS AND DISCUSSION

Synthesis and Characterization of Biosensor. A standard fluorenylmethyloxycarbonyl solid-phase peptide synthesis method was used to obtain TPPP.[22] The synthesis of TPPP was performed as shown in Figure S1, and the validity of TPE−COOH is confirmed in Figure S2. The theoretical molecular weight of TPPP is 2602, while the multicharge peak was found at 1302.98 ($[M + 2H]^{2+}$) in the electrospray ionization mass spectrum (ESI-MS, Figure S3A). Although both TPE and PpIX were extremely hydrophobic, TPPP showed good water solubility due to the introduction of a hydrophilic polyethylene glycol (PEG) segment. A transmission electron microscope (TEM) image revealed that amphiphilic TPPP could self-assemble to form spherical nanoparticles in phosphate-buffered saline (PBS) with a size distribution of 27.9 ± 7.3 nm (Figure 1A). This self-assembly behavior in aqueous solution was due to the fact that TPE and PpIX formed the core due to the hydrophobic interaction, while the PEG segment formed the hydrophilic shell. In addition, a negligible size change of nanoparticles was observed when TPPP was incubated with diluted Dulbecco's modified Eagle medium (DMEM) containing FBS (fetal bovine serum) (Figure S4A), suggesting these nanoparticles would not disassemble or aggregate in the presence of serum proteins. All of these issues ensured that the sub-100 nm nanoparticles could preferentially accumulate in tumor tissue due to the enhanced permeability and retention (EPR) effect.[23] The improved water solubility was further verified by the UV−vis spectrum (Figure 1B). Unlike the free PpIX, which presented a greatly broadened split Soret band (maxima at 352 and 450 nm), a Soret band at around 400 nm was observed in TPPP due to the negligible $\pi-\pi$ stacking.[24]

The improved water solubility of TPPP also accelerated the formation of singlet oxygen ($^1O_2$) under light irradiation. 2′,7′-Dichlorofluorescein diacetate (DCFH-DA) was chosen as the sensor because the nonfluorescent dye DCFH-DA can be rapidly oxidized to 2′,7′-dichlorofluorescein (DCF) with green fluorescence.[25] The fluorescence spectra results showed the fluorescence increase of DCF in the TPPP group was significantly higher than that in the PpIX group due to the fact that the improved solubility of the photosensitizer decreased the aggregation-induced self-quenching behavior (Figure 1C). As a control, undetectable change was observed in the water group. To verify that the enhanced formation $^1O_2$ was related to improved water solubility of the photosensitizer, $(PEG_8)_2$−PpIX was incubated with DCFH-DA. As expected, the fluorescence increase in the $(PEG_8)_2$−PpIX group was also significantly higher than that in the PpIX group (Figure S4B). Similar results were also found in intracellular ROS generation. No green fluorescence or limited green fluorescence was found in blank SCC-7 (squamous cell carcinoma) cells (Figure 1D), TPE-treated cells (Figure 1E), or PpIX-treated SCC-7 cells (Figure 1F). In sharp contrast, significantly brighter green fluorescence was observed in the TPPP group (Figure 1G). The quantitative result of fluorescence intensity revealed that the fluorescence in the TPPP group was nearly 2-fold that in the PpIX group (Figure S5). These results indicate the good ROS generation ability of TPPP.

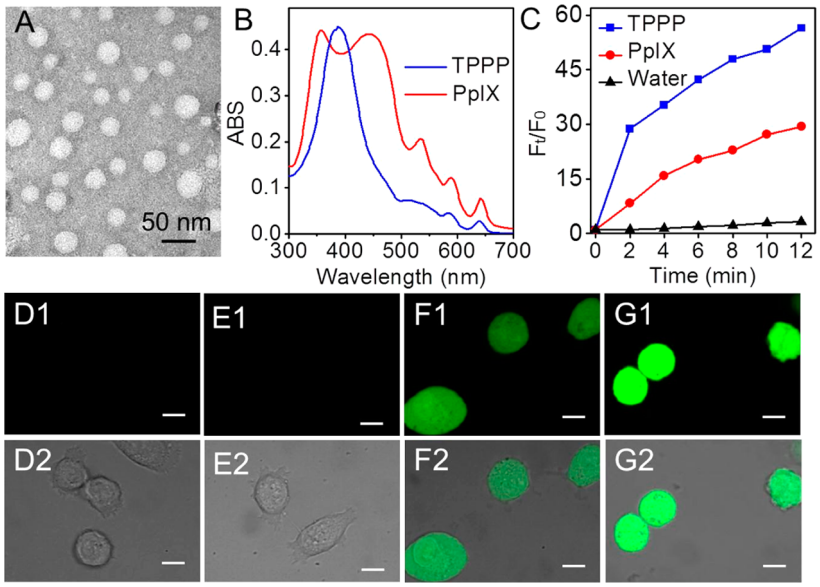

Figure 1. (A) TEM image and (B) UV−vis spectrum of TPPP. (C) ROS production of TPPP with different irradiation times that was measured by the fluorescence spectrum. Water and free PpIX (in 2.5% dimethylsulfoxide (DMSO)) were used as negative controls. Intracellular ROS formation was mediated by various samples: (D1,D2) blank control; (E1,E2) TPE (6.2 mg/L in 2.5% DMSO); (F1,F2) free PpIX (8.6 mg/L in 2.5% DMSO); (G1,G2) TPPP (40 mg/L). The irradiation time was 20 min, and the scale bar is 10 μm. The excitation wavelength of 2′,7′-dichlorofluorescein (DCF) was 488 nm. D1−G1: DCF fluorescence (green) depicted intracellular ROS. D2−G2: Overlay images.

MMP-2 Detection by Fluorescence Spectra. Since TPE was conjugated to PEGylated PpIX with a MMP-2 hydrolyzable substrate PLGVR peptide sequence, it was expected to show MMP-2 responsive AIE. The fluorescence spectra were measured when TPPP was incubated with MMP-2. As shown in Figure 2A, the fluorescence of TPE increased very rapidly with prolonged time when TPPP (80 mg/L) was incubated with 0.4 mg/L of MMP-2. Considering that the fluorescence of TPE was unchangeable with prolonged time in the absence of MMP-2 (Figure S6A), we attributed the rapid fluorescence increase of TPE to the fact that hydrolysis of PLGVR by MMP-2 liberated the TPE molecule, and the enhanced hydrophobicity severely restricted the free rotation of the phenyl group, resulting in aggregation-induced emission.[26] Fluorescence intensity increased more quickly with increasing concentration of MMP-2 (Figure 2B), indicating that the hydrolysis rate of the PLGVR sequence was MMP-2-concentration-dependent.

Furthermore, the fluorescence ratio between TPE and PpIX (F_{TPE}/F_{PpIX}) was investigated when TPPP (80 mg/L) was incubated with various concentrations of MMP-2 for 8 h. We chose the incubation time of 8 h because the fluorescence of TPE could reach a platform at the eighth hour (Figure S6B). It was found that the fluorescence of TPE increased with increased MMP-2 concentration, while the fluorescence of PpIX was stable as an internal reference (Figure 2C). Importantly, a linear relationship was found between the F_{TPE}/F_{PpIX} ratio and concentration of MMP-2 in a certain concentration range (Figure 2D), suggesting that the content of MMP-2 could be reflected by F_{TPE}/F_{PpIX} ratio. According to the crossover point among different trendlines, it was found that the MMP-2 detection limit of TPPP ranged from 0.0065 to 0.303 mg/L. The wide detection range was due to the dramatic fluorescence recovery of TPPP in the presence of MMP-2. In addition, when 0.29 mg/L of MMP-2 was incubated with different concentrations of TPPP, it was found that although the fluorescence of TPE and PpIX changed with the concentration of TPPP (Figure 2E), the F_{TPE}/F_{PpIX} ratio was amazingly stable (Figure 2F), revealing that the relationship between the F_{TPE}/F_{PpIX} ratio and MMP-2 concentration would not be affected by the concentration change of TPPP. Obviously, this ratiometric fluorescence biosensor exhibited great advantages in the accurate and quantitative determination of MMP-2 expression level. Since the retention content of traditional biosensors in the tumor region was unexpectable owing to the individual difference, the enzyme-triggered fluorescence signals of traditional biosensors could only demonstrate the existence of enzymes but not the detailed expression level in practical applications.[27]

Microenvironment Responsive AIE and MMP-2 Detection. The success of ratiometric detection of MMP-2 expression encouraged us to examine whether TPPP could work in living cells. To confirm that TPPP would have contrasting fluorescence emission in response to MMP-2 changes at the cellular level, the fluorescence images were recorded by confocal laser scanning microscopy (CLSM) when 40 mg/L of TPPP was incubated with SCC-7, HT1080 (HT1080 fibrosarcoma cell), HeLa (human cervix carcinoma), and COS7 (African

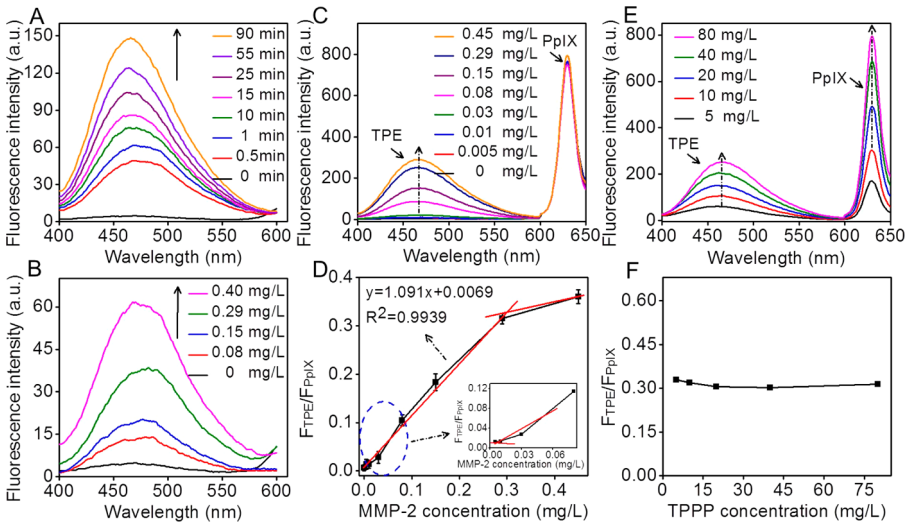

Figure 2. Fluorescence recovery of TPE when TPPP (80 mg/L) was incubated with (A) 0.4 mg/L MMP-2 for different times and (B) various concentrations of MMP-2 for 1 min. (C) Fluorescence spectrum of TPE and PpIX and (D) fluorescence intensity ratios when TPPP (80 mg/L) was incubated with various concentrations of MMP-2 for 8 h. (E) Fluorescence spectrum of TPE and PpIX and (F) fluorescence intensity ratios when TPPP at different concentrations was incubated with 0.29 mg/L of MMP-2 for 8 h. The excitation wavelengths of PpIX and TPE were 409 and 330 nm, respectively.

green monkey SV40-transfected kidney fibroblast) cell lines. These four cell lines were chosen due to the different MMP-2 expression level. Western blotting analysis results demonstrated that the expression of MMP-2 by SCC-7 cells was the highest, while healthy COS7 cells had nearly no MMP-2 expression (Figure 3H,I).[28] As expected, a nearly undetectable blue signal was found in COS7 cells (Figure 3A1). On the contrary, the blue signal of TPE observably increased in tumor cell lines in the following order: HeLa cells ≪ HT1080 cells < SCC-7 cells (Figure 3B1−D1). Meanwhile, the red and blue signals were separated. These findings illustrated that the secreted MMP-2 by tumor cells hydrolyzed the PLGVR sequence in TPPP, leading to the detachment of TPE and PpIX. Then, freed TPE initiated aggregation-induced emission. Meanwhile, higher expression of MMP-2 cleaved more TPPP, resulting in a brighter blue signal. This hydrolysis process of the PLGVR sequence in tumor cells was further verified by adding the MMP-2 inhibitor, 1,10-phenanthroline monohydrate, in SCC-7 cells. It was found that the addition of the MMP-2 inhibitor decreased the blue signal dramatically (Figure 3E1), which substantially confirmed that the generation of the blue signal was due to the secretion of MMP-2. Note that nearly no intensity difference was found in the red signal among different cell lines when the TPPP was 40 mg/L, which indicated that PpIX was perfect as an internal reference. We then calculated the mean fluorescence intensity (MFI) ratio between TPE and PpIX to quantify the results of CLSM. Encouragingly, there existed a high degree of consistency across the MFI ratio (Figure 3G) and Western blotting analysis (Figure 3I). Furthermore, quantitative determination of MMP-2 among these cell lines was also conducted *via* ELISA (enzyme-linked immunosorbent assay). MMP-2 expressions in COS7, HeLa, HT1080, and SCC-7 cell lines (about 3.5×10^5 cells for each cell line) were 0.24 ± 0.11, 0.77 ± 0.35, 2.88 ± 0.30, and 3.69 ± 0.13 ng/mL, respectively. As expected, a similar tendency was observed between the results of quantitative MMP-2 expression and MFI ratio, which substantially indicated that the ratiometric biosensor could accurately detect the MMP-2 expression.

To demonstrate that the MMP-2 expression level was not affected by the biosensor concentration, the concentration of the biosensor was decreased to 20 mg/L. As shown in Figure 3F1,F2, although both the fluorescence intensity of PpIX and TPE decreased to some extent, the blue signal was still obvious. More importantly, the MFI_{TPE}/MFI_{PpIX} ratio had a negligible change when the concentration of the biosensor decreased (Figure 3G), suggesting that the MMP-2 expression level could be reflected by fluorescence ratio regardless of the concentration of the biosensor. Since the expression of MMP-2 was upregulated in many types of tumors, especially malignant tumors, our biosensor exhibited great potential in the recognition of malignant tumors.

On-Demand Photodynamic Therapy. On the basis of the successful recognition of healthy cells from diseased ones *via* the fluorescence ratio, the feasibility of on-demand photodynamic therapeutic efficacy was conducted *via* MTT assay. As shown in Figure 4, TPPP in COS7 cells exhibited undetectable toxicity when no light irradiation was performed. On the contrary, severe toxicity was observed regardless of cell line difference when cells received 30 min of light irradiation, suggesting that the on-demand photodynamic therapy could be realized with ease by regulating the light irradiation condition.[29] Meanwhile, due to the improved

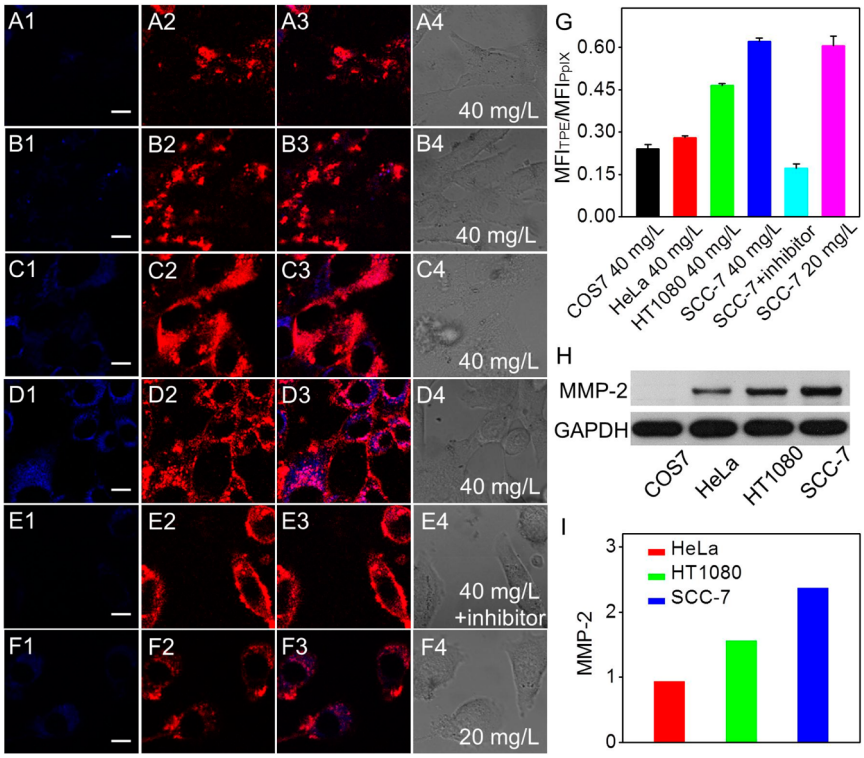

Figure 3. Fluorescence recovery of TPE when 40 mg/L of TPPP was incubated with (A) COS7 cells, (B) HeLa cells, (C) HT1080 cells, and (D) SCC-7 cells; (E) 40 mg/L of TPPP was incubated with SCC-7 cells with MMP-2 inhibitor; (F) 20 mg/L of TPPP was incubated with SCC-7 cells. The excitation wavelengths of PpIX and TPE were 488 and 405 nm, respectively. Blue signal, TPE; red signal, PpIX; A4–F4, bright field. The scale bar is 10 μm. (G) MFI_{TPE}/MFI_{PpIX} values were calculated by ImageJ. (H) Western blotting analysis of MMP-2 among different cell lines and (I) gray values.

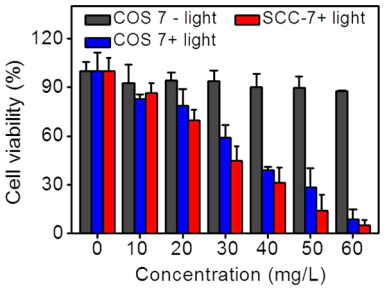

Figure 4. Cytotoxicity of TPPP against SCC-7 cells (with 30 min light irradiation) and COS7 cells (with 30 min or without light irradiation).

solubility, TPPP exhibited greater phototoxicity than free PpIX at a relatively high concentration (Figure S7).

Biosensor Biodistribution, Blood Retention Time, and Tumor Imaging. To confirm that TPPP could achieve MMP-2 overexpressed tumor-specific imaging *in vivo*, we established a SCC-7 tumor-bearing mice model and examined *in vivo* biodistribution and tumor fluorescence imaging (Figure 5). Since PpIX has a long emission wavelengh, the fluorescence of PpIX was traced *via* a small animal imaging system. It was found that this biosensor gradually accumulated in tumor tissue and reached a maximum within 6 h. Subsequently, although the fluorescence decreased with time due to the metabolism, the fluorescence was still observable even after postinjection for 24 h (Figure 5A). Meanwhile, in order to image the fluorescence in the tumor and other organs, the mice were sacrificed at the 24th hour. As shown in Figure 5B, although TPPP accumulated in the primary metabolic organs, liver and kidney inevitably, the greatest amount of TPPP appeared in tumor tissue, and the calculated MFI value revealed that the amount of biosensor in tumor tissue was even slightly higher than that in liver and kidney and significantly higher than that in heart, spleen, lung, and muscle (Figure 5C). These results were attributed to the fact that the EPR-effect-mediated tumor-selective accumulation of nanosized biosensors could successfully trace and image the tumor tissue. To further verify that the PpIX fluorescence accumulated region was the tumor tissue, a two-photon small animal fluorescence imaging technique was utilized to detect the fluorescence recovery of the TPE molecule (Figure 5D). As expected, bright blue fluorescence was observed in the PpIX fluorescence accumulated region, indicating that the tumor biomarker MMP-2 was overexpressed in this tissue, leading to the hydrolysis of the biosensor as well as the fluorescence recovery of TPE. Furthermore, fluorescence of TPE in other tissues was also observed. As shown in Figure S8, no blue signal was found in the heart, and the signals in spleen, lung, and kidney were very weak. Although an observable blue signal was found in the liver,[30] both the fluorescence intensity and area of distribution in the liver

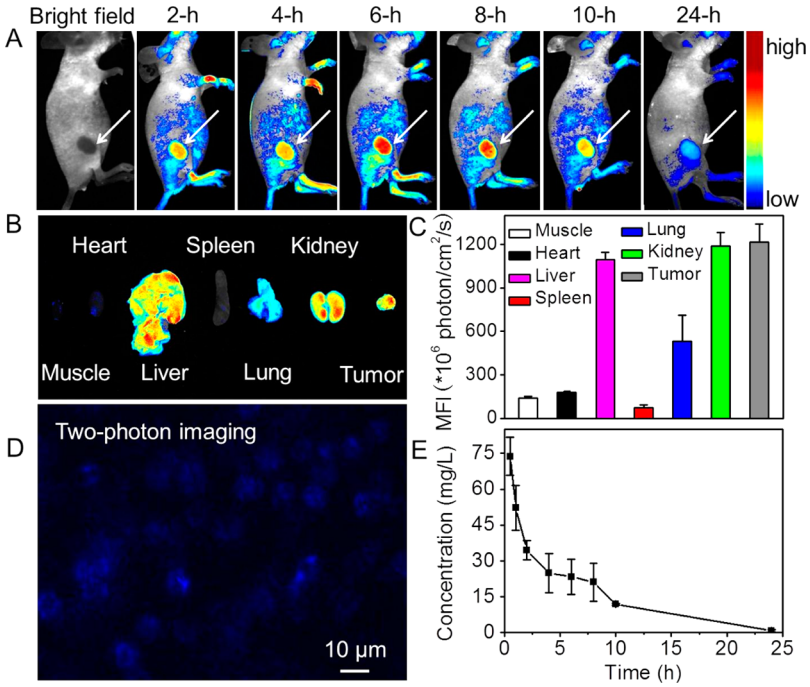

Figure 5. (A) Biodistribution images of SCC-7 tumor-bearing mice after intravenous injection of TPPP, with the white arrow pointing to the tumor tissue. The excitation wavelength of PpIX was 630 nm. (B) Tissue imaging and (C) corresponding MFI values at the 24th hour after postinjection. (D) Two-photon imaging of the tumor tissue while the excitation wavelength was 720 nm for TPE. (E) Blood retention kinetic of TPPP (at 4 mg PpIX equiv·kg^{-1}) after intravenous injection.

were uncomparable to that in the tumor region, indicating the specific MMP-2 responsibility of TPPP in the tumor region. Of particular note was that EPR-induced tumor accumulation of PpIX and MMP-2-triggered AIE precisely imaged the tumor tissue, which provided an appropriate and important irradiation window for photodynamic therapy. It was also found that the accumulation of TPPP in the tumor region was inseparable with the long blood retention time. As shown in Figure 5E, the concentration of TPPP in blood was still very high even up to 8 h; this relatively long blood retention time was probably due to the introduction of a PEG segment[31] and the formation of nanoparticles.[32]

***In Vivo* Photodynamic Therapy Study.** To evaluate whether the efficient tumor accumulation of TPPP leads to enhanced therapeutic efficacy with reduced side effects, SCC-7 tumor-bearing mice were intravenously injected with TPPP solution with or without 20 min light irradiation, and PBS was used as a negative control *via* the tail vein. As shown in Figure 6A, injection of TPPP solution but without light irradiation could not inhibit the tumor growth, which was similar to the results in the PBS group. However, once the mice received certain light irradiation, the growth of the tumor was significantly retarded, suggesting the good antitumor efficacy of TPPP under light irradiation. The above results were also confirmed by the average tumor weight (Figure 6C) and representative tumor images (Figure 6D) at the 11th day (the mice were sacrificed on the 11th day since the tumors in control groups were too big).

In addition, the relative body weight is shown in Figure 6B, and the TPPP group with light irradiation had no obvious weight change, probably due to the negligible systemic toxicity of photodynamic therapy. A series of physiological and biochemical indexes were conducted to evaluate the potential side effects in the liver and kidneys (Figure 6E,F).[33] It was found that there existed negligible differences in the concentration of glutamic pyruvate transaminase and aspartate transaminase among the PBS group and the TPPP group with or without light irradiation, while the creatinine values in all groups were too low to detect, indicating that although TPPP could appear in metabolic organs, liver and kidney, low liver or kidney toxicity was observed due to no irradiation in these regions. As we know, different from the traditional chemical drugs whose undesired side effects were always accompanied by an antitumor effect, the antitumor effect of the photosensitizer could only be activated by light irradiation. On the other hand, ROS had a very limited action distance and short half-life period,[34] and fluorescence imaging-guided precise photodynamic therapy could restrict ROS and phototoxicity in the tumor region furthest, which significantly decreased side effects. The photodynamic therapy with low systemic toxicity was also demonstrated by hematoxylin and eosin (H&E) staining (Figure 6G). Clearly, very few cells were dead in the tumor tissue of the TPPP group without light irradiation. In contrast, a large amount of cells were dead in the tumor tissue of the TPPP group with light irradiation, while undetectable physiological

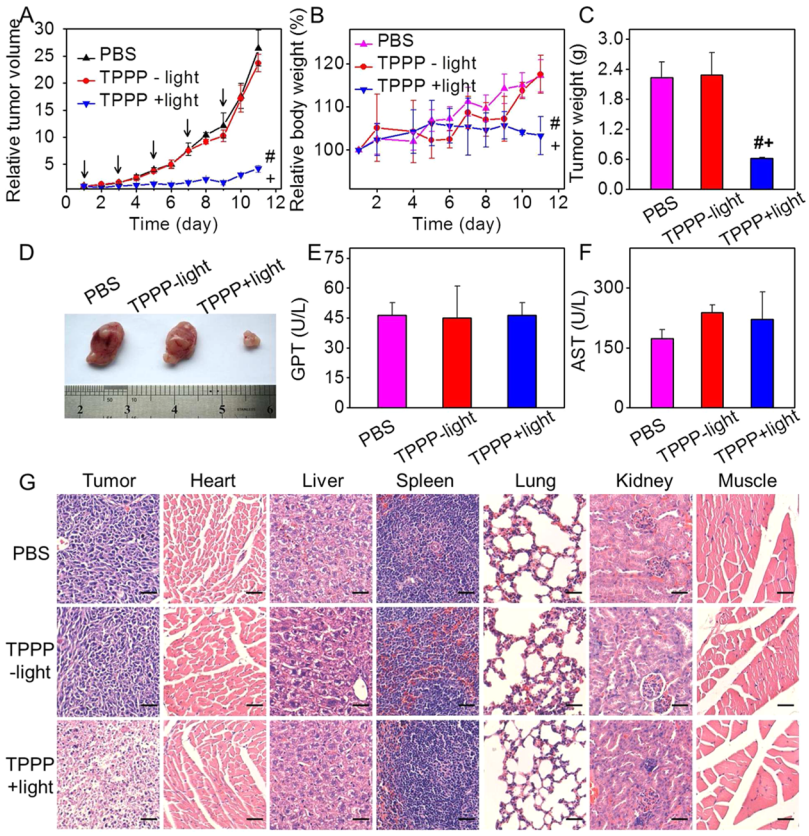

Figure 6. Antitumor study *in vivo via* intravenous injection. (A) Relative tumor volume after post-treatment, with the arrow representing the injection of TPPP solution; (B) relative body weight; (C) average tumor weight; and (D) representative tumor images on the 11th day. Serum levels of (E) glutamic pyruvate transaminase (GPT) and (F) aspartate transaminase (AST) were detected. Every group had six mice; $^{\#}p < 0.05$ and $^{+}p < 0.05$ were determined by a Student's *t* test when the group was compared with the groups that were treated with PBS and TPPP without light irradiation, respectively. (G) H&E staining of tumor tissues and other tissues. The scale bar is 50 μm.

morphology changes were found in the heart, liver, spleen, lungs, kidneys, and muscle tissues.

CONCLUSIONS

In summary, a tumor microenvironment responsive ratiometric biosensor, TPPP, was developed to realize tumor imaging and precise photodynamic antitumor therapy. This ratiometric biosensor successfully differentiated the expression level of MMP-2 among different cell lines regardless of the biosensor concentration according to the fluorescence intensity ratio between TPE and PpIX. Importantly, nanosized TPPP could effectively accumulate in the tumor region *via* EPR effect, and MMP-2 responsive dual fluorescence imaging of both TPE and PpIX pointed out the tumor tissue accurately, which guided the precise photodynamic therapy in the tumor tissue, realizing enhanced therapeutic efficacy with minimal side effects. This strategy opens a window for designing of a ratiometric biosensor for tumor imaging and "precision medicine", which will have great potential in practical treatment.

MATERIALS AND METHODS

Materials. Detailed material information was provided in our previous article.[35] Additionally, PpIX was obtained from Aladdin-Reagent Co. Ltd. (China). DCFH-DA was provided by Beyotime Institute of Biotechnology (China). Fmoc-PEG_8-COOH was provided by Zhoubei Technology Co. Ltd. (Hangzhou, China).

TPE—COOH Synthesis. TPE—COOH was synthesized as described in a previous report.[36] Briefly, under N_2 atmosphere, 4-hydroxybenzophenone (9.5 g, 0.05 mol), benzophenone (9.1 g, 0.05 mol), and zinc powder (8 g, 0.12 mmol) were mixed with 200 mL of tetrahydrofuran at 0 °C. Then, $TiCl_4$ (6.5 mL, 0.06 mmol) was added at 10 °C. The mixture was stirred at room temperature for 0.5 h, followed by reflux overnight. After the mixture was cooled to room temperature, 25 mL of hydrochloric acid (1 mmol/L) was added and extracted with dichloromethane (DCM). The crude product was purified by a silica gel column (DCM/petroleum ether = 3:1), and TPE—OH was obtained. Subsequently, TPE—OH (1.75 g, 5 mmol), *tert*-butylbromoacetate (1 g, 5 mmol), and K_2CO_3 (1 g, 7.5 mmol) were mixed with 25 mL of acetonitrile. The mixture was refluxed overnight. The solution was separated by filtration. The crude product was purified through a silica gel column. This product was added into a solution (DCM/TFA = 1:1) and stirred vigorously for 1.5 h. The solution was poured into DI water and extracted with DCM. The organic layer was concentrated. TPE—COOH was obtained by repeated dissolution and precipitation to remove the trifluoroacetic acid (TFA). TPE—COOH was characterized by electrospray ionization mass spectrometry (ESI-MS) (Finnigan

LCQadvantage) and nuclear magnetic resonance spectroscopy (^{1}H NMR, DMSO-d_6).

TPPP Synthesis. TPPP (TPE-PLGVR$_2$-(PEG$_8$)$_2$-K(PpIX)) was synthesized as described in our previous report.[22] The TPPP was loaded on a rink amide resin (0.51 mmol/g). The amino acid couplings were conducted with Fmoc-protected amino acid, HBTU, and diisopropylethylamine for 2.5 h. During the synthesis, Kaiser reagent was employed to test the coupling efficacy, and 20% piperdine/DMF (v/v) was used to cleave the Fmoc protecting group for two times (10 min + 10 min). After TPE was coupled, the MTT protecting group was selectively moved with 1% TFA in DCM 9 × 5 min. The resin was repeatedly washed with DMF, then PpIX was conjugated to the lateral chain of Lys. Subsequently, TPPP was cleaved from resin in a cleavage cocktail of TFA, triisopropylsilane, and H_2O in the volume ratio of 95:2.5:2.5 for 1.5 h. The product was precipitated in cold ether and collected. TPPP was then dried in vacuum. TPPP was characterized *via* ESI-MS and ^{1}H NMR (DMSO-d_6, Figure S3B).

Cell Culture. SCC-7, HT1080, HeLa, and COS7 cells were incubated in DMEM at 37 °C with a 5% CO_2 atmosphere. The DMEM contained 10% heat-inactivated FBS as well as 1% antibiotics (penicillin−streptomycin, 10 000 U/mL).

TEM Observation. Morphology of TPPP (80 mg/L) was observed by TEM (JEM-2100 microscope). Before observation, TPPP was stained with phosphotungstic acid solution.

Singlet Oxygen Detection. The generation of $^1O_2$ was determined by the fluorescence spectrum as well as CLSM (for intracellular ROS) using DCFH-DA as the sensor. For the fluorescence spectrum, DCFH-DA was pretreated with NaOH and then mixed with TPPP (40 mg/L). The fluorescence spectra were recorded at preset times with an excitation wavelength of 488 nm. PpIX (8.6 mg/L in 2.5% DMSO) was used as a negative control. For CLSM observation, SCC-7 cells were incubated with various samples for 4 h. Then, the medium was replaced. DCFH-DA was added (final concentration 10 μM), and the cells were incubated for 20 min. Light irradiation was performed subsequently (band-pass: 400−700 nm, 3.3 mW/cm^2). The cells were repeatedly washed and then observed as soon as possible *via* CLSM (ex = 488 nm, em = band-pass 500−550 nm).

MMP-2 Enzymatic Response of TPPP. The MMP-2 enzymatic response of AIE fluorescence recovery was investigated by fluorescence spectra at 37 °C. The excitation wavelength of AIE was 330 nm. Briefly, 80 mg/L of TPPP was incubated in the presence or absence of 0.40 mg/mL of MMP-2 (pH 7.4, 10 mM PBS). The fluorescence spectra were recorded at preset times on a LS55 luminescence spectrometer (PerkinElmer). To test the detection sensitivity, 80 mg/L of TPPP solution was incubated with various concentrations of MMP-2, and the fluorescence spectra at 1 min were recorded. The fluorescence intensity ratios between TPE and PpIX at the eighth hour with different concentrations of TPPP or MMP-2 were also determined. The excitation wavelength of PpIX was 409 nm, while the excitation wavelength of TPE was 330 nm.

MMP-2 Detection *via* CLSM. The MMP-2 expression difference among different cell lines was measured *via* CLSM. SCC-7, HT1080, HeLa, and COS7 were chosen as the experiment cell models. Briefly, cells (1 × 10^5 cells/well) were seeded on a 6-well plate. After 24 h, a preset amount of TPPP solution was added. The cells were imaged directly *via* CLSM after being incubated for 8 h. The fluorescence images were determined with a filter set (ex = 405 nm, em = band-pass 450−500 nm) for TPE and a filter set (ex = 488 nm, em = band-pass 600−700 nm) for PpIX. Additionally, to determine the MMP-2 expression, the MMP-2 inhibitor was added 2 h early before TPPP was added. The mean fluorescence intensity of TPE and PpIX was measured by ImageJ software.

Cytotoxicity Assay *in Vitro*. The cytotoxicity of TPPP against SCC-7 and COS7 cells *in vitro* was tested *via* MTT assay. Cells were seeded on a 96-well plate at a density of 6000 cells/well and incubated for 24 h. Then, TPPP at various concentrations was added to each well. After 6 h, the cells received 0 or 30 min light irradiation (3.3 mW/cm^2, 400−700 nm). Cells were incubated for 48 h, and then the medium was replaced with 200 μL of fresh medium. Twenty microliters of MTT was added to each well. Four hours later, the medium was replaced with 200 μL of DMSO. The absorbance at 570 nm was measured by a microplate reader (Bio-Rad, model 550, USA). Cell viability was defined as the percentage of survival cells per total of non-treated cells. All data were averaged from eight independent experiments.

***In Vivo* Optical Imaging, Tissue Distributions, and Pharmacokinetics.** The animal experiments were conducted according to the guidelines for laboratory animals established by the Wuhan University Center for Animal Center Experiment/A3-Lab. SCC-7 tumor model was developed by subcutaneous injection of 1 × 10^6 cells per mouse. SCC-7 tumor-bearing mice were intravenously injected with 200 μL of TPPP solution *via* tail vein (18.5 mg/kg per mouse). At the preset time after injection of TPPP solution, mice were anesthetized and imaged *via* a small animal imaging system. The excitation wavelength was 630 nm, while a long wave fluorescence emission signal (600−700 nm) was collected. For a two-photon-excited fluorescence imaging study, the tumor and other tissues were observed by CLSM at the sixth hour after postinjection; the excitation wavelength was 720 nm, and the fluorescence emission signal (420−500 nm) was collected. For the tissue distribution study, mice were sacrificed at the 24th hour after injection. The tissues, including muscle, heart, liver, spleen, lung, kidney, and tumor, were collected and imaged. For the pharmacokinetic study, mice were injected with TPPP (18.5 mg/kg per mouse) *via* tail vein. The blood samples were obtained at the 0.5, 1, 2, 4, 6, 8, 10, and 24 h time points. Appropriate PBS was added. The samples were repeatedly freeze−thawed and then ultrasonicated for 5 min. The samples were centrifuged at 3000 rpm for 4 min. The fluorescence of the supernatant was determined by fluorescence spectroscopy, while the standard curve was determined *via* the fluorescence spectrum (ex = 409 and ex = 630 nm).

***In Vivo* Systemic Toxicity.** At the 11th day, the blood was extracted from different mice groups. After the blood samples were solidified, the samples were centrifuged at 3000 rpm for 5 min. The serum was collected. The contents of glutamic pyruvate transaminase, aspartate transaminase, and creatinine were detected at Wuhan Xiehe Hospital.

***In Vivo* Antitumor Study.** Mice were injected with 100 μL of SCC-7 cells (1 × 10^6 cells per mouse). When the tumors reached an approximate size of 100 mm^3, the mice were divided into three groups randomly. Each group had six mice. The mice were injected with 200 μL of PBS buffer and TPPP (two groups) at the preset day. Eight hours after being injected, one TPPP group received 20 min light irradiation (630 nm, 220 mW/cm^2), and the other TPPP group received no light irradiation. The dose of PpIX was 4 mg/kg per mouse. The tumor size and mice weight were measured every day. The tumor volume was defined as V = ((tumor length) × (tumor width)^2)/2. Relative tumor volume was calculated as V/V_0 (V_0 was the tumor volume when the treatment was initiated). Relative body weight was defined as M/M_0 (M_0 was the body weight of the mouse when the treatment was initiated). When the mice were sacrificed, the muscle, heart, liver, spleen, lung, kidney, and tumor tissue were collected for further histological examinations *via* H&E staining.

Statistical Analysis. Statistical analysis was performed using a Student's *t* test. The differences were considered to be statistically significant for a p value <0.05.

Conflict of Interest: The authors declare no competing financial interest.

Supporting Information Available: The Supporting Information is available free of charge on the ACS Publications website at DOI: 10.1021/acsnano.5b04243.

Synthetic process of TPPP, ESI-MS spectrum and ^{1}H NMR, TEM image, ROS generation study, fluorescence spectrum of TPPP, cell viability of PpIX against COS7 cells, two-photon imaging of heart, liver, spleen, lung, and kidney (PDF)

Acknowledgment. This work was supported by the National Natural Science Foundation of China (51125014, 51233003, and 21474077) and the Ministry of Science and Technology of China (2011CB606202).

REFERENCES AND NOTES

1. Idris, N. M.; Gnanasammandhan, M. K.; Zhang, J.; Ho, P. C.; Mahendran, R.; Zhang, Y. *In Vivo* Photodynamic Therapy Using Upconversion Nanoparticles as Remote-Controlled Nanotransducers. *Nat. Med.* **2012**, *18*, 1580–1585.
2. Brown, S. Photodynamic Therapy: Two Photons Are Better Than One. *Nat. Photonics* **2008**, *2*, 394–395.
3. Zhang, T.; Lan, R. F.; Chan, C. F.; Law, G. L.; Wong, W. K.; Wong, K. L. *In Vivo* Selective Cancer-Tracking Gadolinium Eradicator as New-Generation Photodynamic Therapy Agent. *Proc. Natl. Acad. Sci. U. S. A.* **2014**, *111*, 5492–5497.
4. Sanabria, L. M.; Rodríguez, M. E.; Cogno, I. S.; Vittar, N. B. R.; Pansa, M. F.; Lamberti, M.; Rivarola, V. A. Direct and Indirect Photodynamic Therapy Effects on the Cellular and Molecular Components of the Tumor Microenvironment. *Biochim. Biophys. Acta, Rev. Cancer* **2013**, *1835*, 36–45.
5. Pan, L. M.; Liu, J. N.; Shi, J. L. Intranuclear Photosensitizer Delivery and Photosensitization for Enhanced Photodynamic Therapy with Ultralow Irradiance. *Adv. Funct. Mater.* **2014**, *24*, 7318–7327.
6. Cheng, Y.; Morshed, R. A.; Auffinger, B.; Tobias, A. L.; Lesniak, M. S. Multifunctional Nanoparticles for Brain Tumor Imaging and Therapy. *Adv. Drug Delivery Rev.* **2014**, *66*, 42–57.
7. Ethirajan, M.; Chen, Y. H.; Joshi, P.; Pandey, R. K. The Role of Porphyrin Chemistry in Tumor Imaging and Photodynamic Therapy. *Chem. Soc. Rev.* **2011**, *40*, 340–362.
8. Lindner, U.; Trachtenberg, J.; Lawrentschuk, N. Focal Therapy in Prostate Cancer: Modalities, Findings and Future Considerations. *Nat. Rev. Urol.* **2010**, *7*, 562–571.
9. Chen, D. Q.; Wang, C.; Nie, X.; Li, S. M.; Li, R. M.; Guan, M. R.; Liu, Z.; Chen, C. Y.; Wang, C. R.; Wan, L. J.; et al. Photoacoustic Imaging Guided Near-Infrared Photothermal Therapy Using Highly Water-Dispersible Single-Walled Carbon Nanohorns as Theranostic Agents. *Adv. Funct. Mater.* **2014**, *24*, 6621–6628.
10. Zheng, G.; Chen, J.; Stefflova, K.; Jarvi, M.; Li, H.; Wilson, B. C. Photodynamic Molecular Beacon as an Activatable Photosensitizer Based on Protease-Controlled Singlet Oxygen Quenching and Activation. *Proc. Natl. Acad. Sci. U. S. A.* **2007**, *104*, 8989–8994.
11. Wüstner, D.; Solanko, L. M.; Lund, F. W.; Sage, D.; Schroll, H. J.; Lomholt, M. A. Quantitative Fluorescence Loss in Photobleaching for Analysis of Protein Transport and Aggregation. *BMC Bioinf.* **2012**, *13*, 296–317.
12. Chen, Y. C.; Zhu, C. C.; Yang, Z. H.; Chen, J. J.; He, Y. F.; Jiao, Y.; He, W. J.; Qiu, L.; Cen, J. J.; Guo, Z. J. A Ratiometric Fluorescent Probe for Rapid Detection of Hydrogen Sulfide in Mitochondria. *Angew. Chem.* **2013**, *125*, 1732–1735.
13. Myochin, T.; Kiyose, K.; Hanaoka, K.; Kojima, H.; Terai, T.; Nagano, T. Rational Design of Ratiometric Near-Infrared Fluorescent pH Probes with Various pKa Values, Based on Aminocyanine. *J. Am. Chem. Soc.* **2011**, *133*, 3401–3409.
14. Tsai, Y. T.; Zhou, J.; Weng, H.; Shen, J. H.; Tang, L. P.; Hu, W. J. Real-Time Noninvasive Monitoring of *in Vivo* Inflammatory Responses Using a pH Ratiometric Fluorescence Imaging Probe. *Adv. Healthcare Mater.* **2014**, *3*, 221–229.
15. Albers, A. E.; Okreglak, V. S.; Chang, C. J. A FRET-Based Approach to Ratiometric Fluorescence Detection of Hydrogen Peroxide. *J. Am. Chem. Soc.* **2006**, *128*, 9640–9641.
16. Shi, P.; Liu, Z.; Dong, K.; Ju, E. G.; Ren, J. S.; Du, Y. D.; Li, Z. Q.; Qu, X. G. A Smart "Sense-Act-Treat" System: Combining a Ratiometric pH Sensor with a Near Infrared Therapeutic Gold Nanocage. *Adv. Mater.* **2014**, *26*, 6635–6641.
17. Tian, J. W.; Ding, L.; Ju, H. X.; Yang, Y. C.; Li, X. L.; Shen, Z.; Zhu, Z.; Yu, J. S.; Yang, C. Y. J. A Multifunctional Nanomicelle for Real-Time Targeted Imaging and Precise Near-Infrared Cancer Therapy. *Angew. Chem., Int. Ed.* **2014**, *53*, 9544–9549.
18. Savariar, E. N.; Felsen, C. N.; Nashi, N.; Jiang, T.; Ellies, L. G.; Steinbach, P.; Tsien, R. Y.; Nguyen, Q. T. Real-Time *in Vivo* Molecular Detection of Primary Tumors and Metastases with Ratiometric Activatable Cell-Penetrating Peptides. *Cancer Res.* **2013**, *73*, 855–864.
19. Leung, C. W. T.; Hong, Y. N.; Chen, S. J.; Zhao, E. G.; Lam, J. W. Y.; Tang, B. Z. A Photostable AIE Luminogen for Specific Mitochondrial Imaging and Tracking. *J. Am. Chem. Soc.* **2013**, *135*, 62–65.
20. Ding, D.; Li, K.; Liu, B.; Tang, B. Z. Bioprobes Based on AIE Fluorogens. *Acc. Chem. Res.* **2013**, *46*, 2441–2453.
21. Rananaware, A.; Bhosale, R. S.; Patil, H.; Al Kobaisi, M.; Abraham, A.; Shukla, R.; Bhosale, S. V.; Bhosale, S. V. Precise Aggregation-Induced Emission Enhancement *via* H^+ Sensing and Its Use in Ratiometric Detection of Intracellular pH Values. *RSC Adv.* **2014**, *4*, 59078–59082.
22. Chen, C. S.; Xu, X. D.; Wang, Y.; Yang, J.; Jia, H. Z.; Cheng, H.; Chu, C. C.; Zhuo, R. X.; Zhang, X. Z. A Peptide Nanofibrous Indicator for Eye-Detectable Cancer Cell Identification. *Small* **2013**, *9*, 920–926.
23. Cabral, H.; Matsumoto, Y.; Mizuno, K.; Chen, Q.; Murakami, M.; Kimura, M.; Terada, Y.; Kano, M. R.; Miyazono, K.; Kataoka, K.; et al. Accumulation of Sub-100 nm Polymeric Micelles in Poorly Permeable Tumours Depends on Size. *Nat. Nanotechnol.* **2011**, *6*, 815–823.
24. Ding, H. Y.; Sumer, B. D.; Kessinger, C. W.; Dong, Y.; Huang, G.; Boothman, D. A.; Gao, J. M. Nanoscopic Micelle Delivery Improves the Photophysical Properties and Efficacy of Photodynamic Therapy of Protoporphyrin IX. *J. Controlled Release* **2011**, *151*, 271–277.
25. Han, K.; Lei, Q.; Wang, S. B.; Hu, J. J.; Qiu, W. X.; Zhu, J. Y.; Yin, W. N.; Luo, X.; Zhang, X. Z. Dual-Stage-Light-Guided Tumor Inhibition by Mitochondria-Targeted Photodynamic Therapy. *Adv. Funct. Mater.* **2015**, *25*, 2961–2971.
26. Shi, H. B.; Kwok, R. T. K.; Liu, J. Z.; Xing, B. G.; Tang, B. Z.; Liu, B. Real-Time Monitoring of Cell Apoptosis and Drug Screening Using Fluorescent Light-up Probe with Aggregation-Induced Emission Characteristics. *J. Am. Chem. Soc.* **2012**, *134*, 17972–17981.
27. Chang, C. J.; Jaworski, J.; Nolan, E. M.; Sheng, M.; Lippard, S. J. A Tautomeric Zinc Sensor for Ratiometric Fluorescence Imaging: Application to Nitric Oxide-Induced Release of Intracellular Zinc. *Proc. Natl. Acad. Sci. U. S. A.* **2004**, *101*, 1129–1134.
28. Lee, S.; Cha, E. J.; Park, K.; Lee, S. Y.; Hong, J. K.; Sun, I. C.; Kim, S. Y.; Choi, K.; Kwon, I. C.; Ahn, C. H.; et al. A Near-Infrared-Fluorescence-Quenched Gold-Nanoparticle Imaging Probe for *in Vivo* Drug Screening and Protease Activity Determination. *Angew. Chem.* **2008**, *120*, 2846–2849.
29. Wang, B.; Yuan, H. X.; Liu, Z.; Nie, C. Y.; Liu, L. B.; Lv, F. T.; Wang, Y. L.; Wang, S. Cationic Oligo (p-Phenylene Vinylene) Materials for Combating Drug Resistance of Cancer Cells by Light Manipulation. *Adv. Mater.* **2014**, *26*, 5986–5990.
30. Akers, W. J.; Xu, B. G.; Lee, H.; Sudlow, G. P.; Fields, G. B.; Achilefu, S.; Edwards, W. B. Detection of MMP-2 and MMP-9 Activity *in Vivo* with a Triple-Helical Peptide Optical Probe. *Bioconjugate Chem.* **2012**, *23*, 656–663.
31. Gref, R.; Domb, A.; Quellec, P.; Blunk, T.; Müller, R. H.; Verbavatz, J. M.; Langer, R. The Controlled Intravenous Delivery of Drugs Using PEG-Coated Sterically Stabilized Nanospheres. *Adv. Drug Delivery Rev.* **2012**, *64*, 316–326.
32. Huang, P.; Wang, D. L.; Su, Y.; Huang, W.; Zhou, Y. F.; Cui, D. X.; Zhu, X. Y.; Yan, D. Y. Combination of Small Molecule Prodrug and Nanodrug Delivery: Amphiphilic Drug-Drug Conjugate for Cancer Therapy. *J. Am. Chem. Soc.* **2014**, *136*, 11748–11756.
33. Tang, K.; Zhang, Y.; Zhang, H. F.; Xu, P. W.; Liu, J.; Ma, J. W.; Lv, M.; Li, D. P.; Katirai, F.; Huang, B.; et al. Delivery of Chemotherapeutic Drugs in Tumour Cell-Derived Microparticles. *Nat. Commun.* **2012**, *3*, 1282–1293.
34. Han, K.; Lei, Q.; Jia, H. Z.; Wang, S. B.; Yin, W. N.; Chen, W. H.; Cheng, S. X.; Zhang, X. Z. A Tumor Targeted Chimeric Peptide for Synergistic Endosomal Escape and Therapy by Dual-Stage Light Manipulation. *Adv. Funct. Mater.* **2015**, *25*, 1248–1257.
35. Han, K.; Liu, Y.; Yin, W. N.; Wang, S. B.; Xu, Q.; Zhuo, R. X.; Zhang, X. Z. A FRET-Based Dual-Targeting Theranostic Chimeric Peptide for Tumor Therapy and Real-Time

Apoptosis Imaging. *Adv. Healthcare Mater.* **2014**, *3*, 1765–1768.
36. Wang, H. B.; Huang, Y.; Zhao, X. P.; Gong, W.; Wang, Y.; Cheng, Y. Y. A Novel Aggregation-Induced Emission Based Fluorescent Probe for an Angiotensin Converting Enzyme (ACE) Assay and Inhibitor Screening. *Chem. Commun.* **2014**, *50*, 15075–15078.